

**Measurement of Inclusive  
and Diffractive  
Electromagnetic Jet  
Transverse Single-Spin  
Asymmetry in Polarized  
p+p Collision at  $\sqrt{s} = 200$   
GeV at STAR**

Latif Kabir, Xilin Liang<sup>1</sup>

October 7, 2022

<sup>1</sup>email: [xilin.liang@email.ucr.edu](mailto:xilin.liang@email.ucr.edu)

# Contents

<b>1</b>	<b>Introduction</b>	<b>5</b>
<b>2</b>	<b>Dataset</b>	<b>7</b>
2.1	General information . . . . .	7
2.2	Triggers . . . . .	7
2.3	Electromagnetic jet reconstruction . . . . .	8
<b>3</b>	<b>Data Quality Assurance (QA)</b>	<b>9</b>
<b>4</b>	<b>Event Selection</b>	<b>12</b>
4.1	EM-jet cut . . . . .	13
4.2	Event property cut . . . . .	14
4.3	Roman Pot track cut . . . . .	14
4.4	Background cut . . . . .	16
<b>5</b>	<b>Corrections</b>	<b>21</b>
5.1	Underlying Event (UE) correction . . . . .	21
5.1.1	Underlying Event energy correction for diffractive process	21
5.1.2	Underlying Event energy correction for inclusive process .	22
5.2	Detector level to particle level EM-jet energy correction . . . . .	22
<b>A</b>	<b>Roman Pot simulation</b>	<b>23</b>
<b>B</b>	<b>FMS simulation</b>	<b>27</b>

# List of Figures

1.1	General analysis procedures for inclusive and diffractive EM-jet $A_N$ analyses . . . . .	6
3.1	Example of EM-jet distribution at FMS before additional hot channel masking. The red color area in this plot indicates the possible hot channels. . . . .	10
3.2	Example of EM-jet distribution at FMS after additional hot channel masking. . . . .	11
4.1	Bunch crossing distribution for run 16088023 as example. Left plot shows the blue beam bunch crossing distribution; right plot shows the yellow beam bunch crossing distribution. The abort gap for both blue beam and yellow beam are with bunch ID [31, 39] and [111, 119]. . . . .	15
4.2	2 possible channels for diffractive processes. . . . .	17
4.3	Distribution of the east side RP track $\theta_x$ (left plot) and $\theta_y$ (right plot) . . . . .	17
4.4	Distribution of the west side RP track $\theta_x$ (left plot) and $\theta_y$ (right plot) . . . . .	18
4.5	Sum energy distribution for EM-jet with $0.1 < x_F < 0.45$ , but separate by 5 different $x_F$ region. . . . .	19
4.6	Distribution of sum energy vs west side small BBC ADC sum (left plot) and sum energy vs west side large BBC ADC sum (right plot). The region with sum energy $> 108$ GeV is considered as background and the region with sum energy $< 108$ GeV is considered as signal. . . . .	20
4.7	Distribution of signals to backgrounds by every small BBC ADC sum bin (left) and by every large BBC ADC sum bin (right). The red vertical line indicate the proper cut for small (large) BBC ADC sum. . . . .	20

5.1	UE distribution for diffractive EM-jet analysis. The left plot shows the subtraction term $\rho \times A$ . The right plot shows the EM-jet energy distribution after the UE correction. . . . .	22
A.1	Number of silicon planes that the west side RP track hits. . . . .	24
A.2	Number of silicon planes that the east side RP track hits. . . . .	25
A.3	Distribution of the only east side RP track $\theta_x$ (left plot) and $\theta_y$ (right plot) . . . . .	25
A.4	Distribution of the only west side RP track $\theta_x$ (left plot) and $\theta_y$ (right plot) . . . . .	26

# List of Tables

2.1	Trigger name lists and trigger ID for run 15 . . . . .	8
4.1	4 acceptable 4-bit spin patterns . . . . .	14
4.2	Sum energy cut for different $x_F$ bins . . . . .	18

# 1 Chapter 1

## 2 Introduction

3 Transverse single-spin asymmetries ( $A_N$ ), which are defined as left-right asym-  
4 metries of the particle production with respect to the plane defined by the  
5 momentum and spin directions of the polarized beam, have been observed to be  
6 large for charged- and neutral-hadron production in hadron-hadron collisions  
7 over a couple of decades [1, 2, 3, 4, 5]. In pQCD, however, the  $A_N$  is predicted  
8 to be small and close to zero in high energy collisions [6]. There are two major  
9 frameworks that can provide a potential explanation for such sizeable asymme-  
10 tries. The first one is the transverse-momentum-dependent (TMD) contribu-  
11 tions from the initial-state quark and gluon Sivers functions and/or the final-  
12 state Collins fragmentation functions. In the Sivers mechanism, the asymmetry  
13 comes from the correlation between the proton spin and the parton transverse  
14 momentum [7], while the Collins effect arises from the correlation between the  
15 spin of the fragmenting quark and the outgoing hadron's transverse momentum  
16 [8]. Another framework is based on the twist-3 contributions in the collinear  
17 factorization framework, including the quark-gluon or gluon-gluon correlations  
18 and fragmentation functions [9].

19 According to the study by CMS Collaboration [11], diffractive interactions  
20 contribute to about a significant fraction ( $\sim 25\%$ ) of the total inelastic p+p  
21 cross section at high energies. The simulation for hard diffractive events based  
22 on PYTHIA-8 predicts that the fraction of diffractive cross section in the total  
23 inclusive cross section at the forward region is about 20% [4]. In recent years,  
24 analyses of  $A_N$  for forward  $\pi^0$  and electromagnetic jets (EM-jets) in  $p^\uparrow + p$   
25 collisions at STAR indicated that there might be non-trivial contributions to  
26 the large  $A_N$  from diffractive processes [5, 10]. Measuring the  $A_N$  of diffractive  
27 process will provide an opportunity to study the properties and understand the  
28 diffractive exchange in p+p collisions.

29 The analyses consist of two parts: inclusive EM-jet  $A_N$  at run 15 FMS

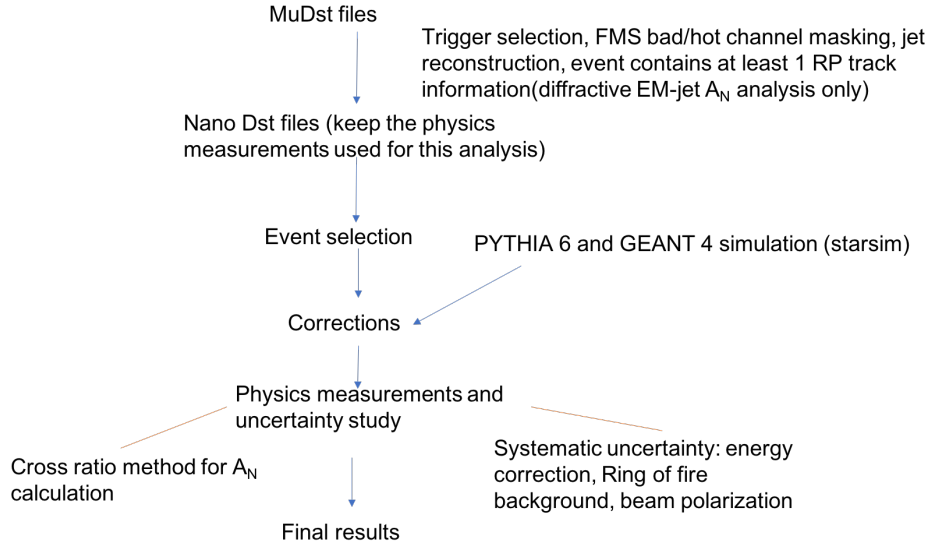


Figure 1.1: General analysis procedures for inclusive and diffractive EM-jet  $A_N$  analyses

30 and diffractive EM-jet  $A_N$  at run 15 FMS. Compared to the previously STAR  
 31 published paper [5], the former analysis on focuses on inclusive EM-jet  $A_N$  for  
 32 the dependence on photon multiplicity inside the EM-jet, EM-jet transverse  
 33 momentum ( $p_T$ ) and energy. The later analysis is the first measurement for  
 34 diffractive EM-jet  $A_N$  at STAR.

35 The structure of the analysis note follows the analysis procedures in Fig.(1.1).  
 36 Chapter 2 will present the dataset. Chapter 3 will present the data quality as-  
 37 surance (QA). Chapter 4 will present the event selection. Chapter 5 will present  
 38 the corrections. Chapter 6 will present the systematic uncertainty. Chapter 7  
 39 will present the final results.

## 40 Chapter 2

# 41 Dataset

### 42 2.1 General information

43 The inclusive and diffractive EM-jet  $A_N$  analyses both utilize polarized p+p  
44 collision at  $\sqrt{s} = 200$  GeV taken in run 15. Details of the data set are listed as  
45 follow:

- 46 • Trigger setup name: production\_pp200trans\_2015
- 47 • Data stream: fms
- 48 • Production tag: P15ik
- 49 • File type: MuDst files in Distributed Disk (DD)

50 The list of MuDst files is saved in ??? The filelists are kept in a fill-by-fill  
51 basis, where fill is the unit of the injection and store cycle of the proton beams  
52 at RHIC.

53 Both analyses generate smaller size data stream files (DST) from the MuDst  
54 files, applying trigger filter (described in Section 2.2) and jet reconstruction  
55 (described in Section 2.3). In addition, the events with at least one Roman Pot  
56 track are required for diffractive EM-jet  $A_N$  analysis when generating the DST  
57 files.

### 58 2.2 Triggers

59 9 triggers for FMS are used for both analyses. The triggers with their ID are  
60 listed in Table (2.1). However, the FMS-sm-bs2 trigger is considered as a source  
61 of background and excluded from the trigger list in the final results. Details can  
62 be seen in ???.



Table 2.1: Trigger name lists and trigger ID for run 15

Trigger name	Trigger ID
FMS-JP0	480810 / 480830
FMS-JP1	480809 / 480829
FMS-JP2	480808 / 480828
FMS-sm-bs0	480801 / 480821 / 480841
FMS-sm-bs1	480802 / 480822
FMS-sm-bs2	480803 / 480823 / 480843
FMS-lg-bs0	480804 / 480824 / 480844
FMS-lg-bs1	480805 / 480825
FMS-lg-bs2	480806 / 480826

### 63 2.3 Electromagnetic jet reconstruction

64 The Electromagnetic jets (EM-jets) are the jet consisting of only photon. The  
65 photon candidates for EM-jets reconstruction are the FMS points. The FMS  
66 points are formed by the shower shape fitting for the FMS clusters, where the  
67 FMS clusters are the groups of adjacent FMS hits by FMS cluster finding al-  
68 gorithm. The hits are the basic reconstructed object in the FMS, which are  
69 formed by the towers with non-zero ADC value [12].

70 In order to reduce the noise background, the FMS points with  $E > 2GeV$   
71 and  $E_T > 0.2GeV$  are considered in the analysis. The EM-jets are reconstructed  
72 with the anti- $k_T$  algorithm from the FastJet package [13], with the resolution  
73 parameter  $R = 0.7$ . The primary vertex of the EM-jets are determined according  
74 to the priority of TPC vertex, BBC vertex and VPD vertex. If the primary  
75 vertex is unable to determined among these three detectors, it will set to be  
76  $(0,0,0)$ .

77 Figure (xxx) shows the EM-jet kinematic for the inclusive process.

## 78 Chapter 3

# 79 Data Quality Assurance 80 (QA)

81 The calibration and quality assurance for run 15 FMS dataset are from STAR  
82 framework [14], but with some additional steps. They mainly include the fol-  
83 lowing items:

- 84 • Bit shift (BS): It refers to the binary bit, used to store the ADC value,  
85 not starting from the normal lowest bit. The BS will affect a cell's ADC  
86 distribution and the corresponding hit energy. The approach to check the  
87 BS is to use the ADC of each FMS hit to check with its corresponding BS  
88 value of the cell [15].
- 89 • Gain and gain correction: The energy of the hit =  $\text{ADC} \times \text{gain} \times \text{gain}$   
90 correction. The gain is the calculated value based on a cell's  $\eta$  position,  
91 while the gain correction is obtained from offline calibration [14]. The flag  
92 of the gain and the gain correction for each tower in the STAR database  
93 is "fmsGainCorr-BNL-C".
- 94 • Hot channel and bad channel masking: A hot channel refers to the tower  
95 with a number of hits far more than the average number of hits for the  
96 whole detector towers within some time range. A bad channel refers to the  
97 problematic towers which might be suffered from hardware issues. Both  
98 hot channels and bad channels can affect the quality of the calibration  
99 and the analyses since there are quite a lot of not physical signals con-  
100 taminated. To mask out these channels, the gain values are set to zero.  
101 In addition to the existing hot channel and bad channel masking from  
102 STAR calibration [14], the fill-by-fill hot channel masking is applied in  
103 both analyses. The EM-jet distribution before any event selections for

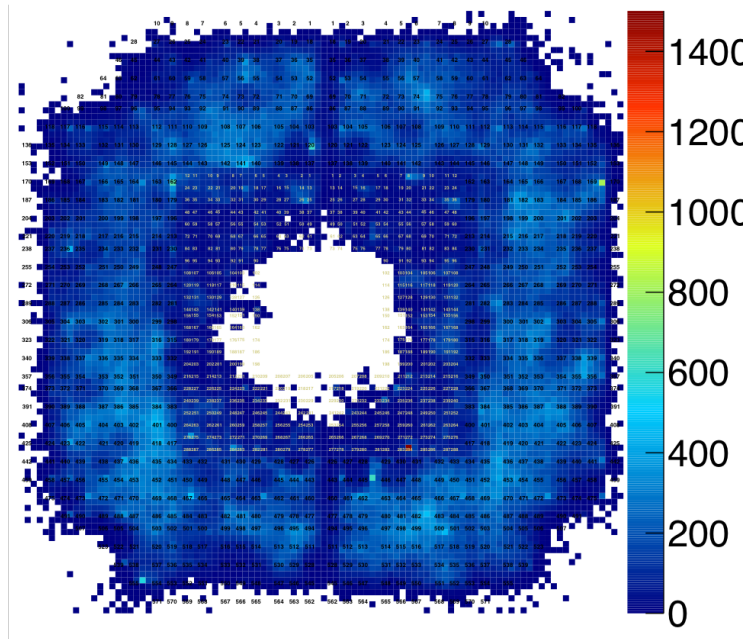


Figure 3.1: Example of EM-jet distribution at FMS before additional hot channel masking. The red color area in this plot indicates the possible hot channels.

104 every fill is checked to find out any possible hot channels. Figure (3.1)  
 105 shows one example of the EM-jet distribution at the FMS. The areas with  
 106 extremely high EM-jet entries compared to the overall average entries in  
 107 the plot are assumed to be the hot channel area. The channels within  
 108 these areas are considered hot channels and added manually to the hot  
 109 channel lists. Figure (3.2) shows the EM-jet distribution for fill 18827 as  
 110 an example after the additional hot channel masking. From the plot, the  
 111 hot channels disappear and the entries of the majority of towers are close  
 112 to the average entries.

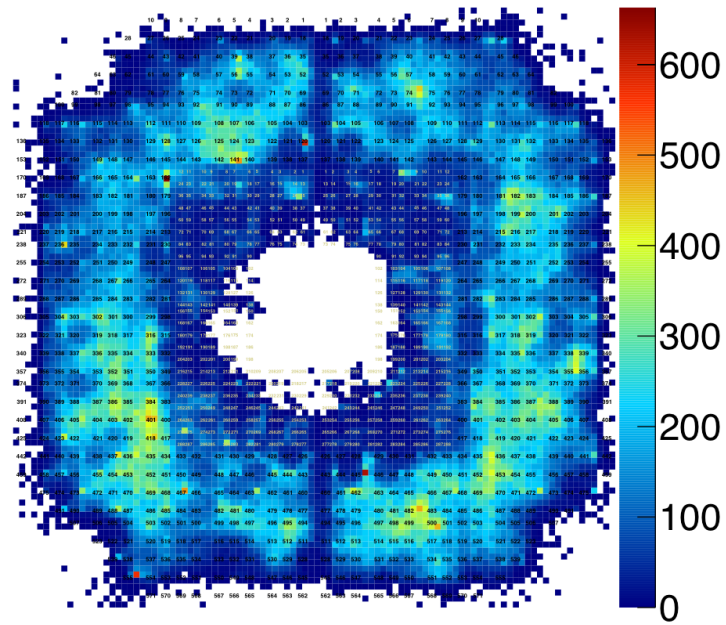


Figure 3.2: Example of EM-jet distribution at FMS after additional hot channel masking.

## 113 Chapter 4

# 114 Event Selection

115 The event selections for inclusive and diffractive EM-jets include the following  
116 items:

- 117 1. Triggers: The triggers used for both analyses are the FMS BS triggers and  
118 FMS JP triggers. They are listed in Table(2.1). Only the events with any  
119 triggers fired are kept.
- 120 2. EM-jet reconstruction: EM-jets are reconstructed by FMS point by Anti-  
121  $k_T$  algorithm with  $R = 0.7$ . The FMS points are required to have  $E > 2$   
122 GeV and  $E_T > 0.2$  GeV. Details of the EM-jet reconstruction are in Section  
123 (2.3)
- 124 3. EM-jet cut: Details of the EM-jet cuts are in Section (4.1)
  - 125 • The EM-jets for inclusive EM-jet analysis are required to have  $p_T > 2$   
126 GeV, while the EM-jets for diffractive EM-jet analysis are required  
127 to have  $p_T > 1$  GeV.
  - 128 • The vertex  $z$  are within  $[-80, 80]$  cm.
  - 129 • The pseudorapidity ( $\eta$ ) of the EM-jets are within  $[2.8, 3.8]$  for inclu-  
130 sive EM-jet analysis and  $[2.6, 4.1]$  for diffractive EM-jet analysis.
  - 131 • The event with EM-jet  $|x_F| > 1$  or  $E > 100$  GeV are excluded.
  - 132 • The number of EM-jets for each event is not zero.
- 133 4. Event property cut: Details of the event property cuts are in Section (4.2)
  - 134 • Veto on abort gap.
  - 135 • The spin status for the blue beam and yellow beam is correct and  
136 accept the 4 cases of 4-bit spin patterns.

- 137 5. Roman Pot (RP) track cut: These cuts are only used for diffractive EM-jet  
138 analysis. Details are in Section (4.3)
- 139 • Only accept the event with the following 2 cases: no east side RP  
140 track and only one west side RP track; only one east side RP track  
141 and only one west side RP track.
  - 142 • Each RP track must hit at least 7 RP silicon planes.
  - 143 • Each RP track must satisfy  $-2 < \theta_x < 2$  mrad and  $1.5 < |\theta_y| < 4.5$   
144 mrad.
- 145 6. Background cut: Details of the background cut are in Section (4.4).
- 146 • Ring of fire cut (for both analyses): Exclude FMS-sm-bs3 trigger.
  - 147 • sum energy cut (only for diffractive EM-jet analysis): Cut on the sum  
148 of west side RP track energy and EM-jet energy. Details in Table  
149 (???)
  - 150 • West BBC ADC sum cut (only for diffractive EM-jet analysis): west  
151 side large BBC ADC sum  $< 80$  and west side small BBC ADC sum  
152  $< 100$ .
- 153 7. Corrections: Apply EM-jet energy correction (details in Sector(???)) and  
154 Underlying-Event (UE) correction (details in Sector(???))

## 155 4.1 EM-jet cut

156 The EM-jet reconstruction is based on the anti- $k_T$  algorithm by the FastJet  
157 package, with the R parameter 0.7, which is described in 2.3. To reduce the  
158 background EM-jet, the  $p_T$  cut is applied. For the inclusive EM-jet, the cut is  
159  $p_T < 2$  GeV. However, the diffractive process applies the cut on EM-jet  $p_T < 1$   
160 GeV, due to the limited statistics for this process.

161 The EM-jet vertex is determined by the primary vertex following the priority  
162 of TPC, BBC ,and VPD. If the primary vertex can be obtained by TPC, the  
163 TPC vertex will be the primary vertex. Otherwise, check the BBC vertex on  
164 the next step. If there is no BBC vertex, then check the VPD vertex. If there  
165 is still no VPD vertex, the primary vertex is set to be  $z=0$ . The vertex  $z$  cut on  
166  $|z| < 80$  cm is considered for both inclusive and diffractive processes.

167 In addition, we apply the cut on EM-jet  $\eta$  which aims to get rid of the bad  
168 reconstructed EM-jets and the EM-jets hitting outside the FMS. Therefore, the  
169 EM-jet cut are [2.8, 3.8] for inclusive EM-jet analysis and [2.6, 4.1] for diffractive  
170 EM-jet analysis.

Table 4.1: 4 acceptable 4-bit spin patterns

4-bit spin	Translate	Blue beam polarization	Yellow beam polarization
0101	5	up	up
0110	6	up	down
1001	9	down	up
1010	10	down	down

171 Also, the events with EM-jet energy  $E > 100$  GeV or  $|x_F| > 1$  are discarded,  
 172 where Feynman-x  $x_F$  can be estimated by the EM-jet energy divided by the  
 173 beam energy ( $x_F = \frac{2E}{\sqrt{s}}$ ). Those events are possibly pile-up events.

174 Finally, the events are required to have non-zero EM-jets. Although those  
 175 events with zero EM-jets are not counted in the EM-jet yield when calculating  
 176 the  $A_N$ , they still have effects in polarization calculation, which have some  
 177 effects on the final  $A_N$  results. Applying the non-zero EM-jet cuts will solve  
 178 this issue and calculate the precise polarization.

## 179 4.2 Event property cut

180 The abort gap for both blue beam and yellow beam is within bunch ID [31, 39]  
 181 and [111, 119] for run 15. Figure (4.1) shows one example of bunch crossing  
 182 distribution for one physics run. The bunches with low entries are the abort  
 183 gap. The events with either blue beam or yellow beam with the abort gap are  
 184 discarded.

185 The spin patterns for each beam, either up or down, are obtained from the  
 186 bunch crossing of each event. The translation from the database for the spin  
 187 patterns is described in [16]. The spin patterns for both blue and yellow beam  
 188 are combined as 4-spin bit. The events satisfying the following 4 4-spin bit  
 189 cases in Table (4.1) are considered in both analyses. These patterns require the  
 190 polarization of both blue and yellow beam either up or down.

## 191 4.3 Roman Pot track cut

192 Roman Pot (RP) detector is used for detecting the slightly scattered proton  
 193 along the beam. The RP tracks are generally recognized as slightly scattered  
 194 protons. To identify the diffractive process, the coincidence between the FMS  
 195 detector and RP detector is required, which can satisfy the requirement of the  
 196 presence of the rapidity gap for the diffractive process. Therefore, two possible  
 197 channels are considered for the diffractive processes, which can be shown in  
 198 Figure (4.2). Figure (4.2 top) shows the diffractive channel requiring no east

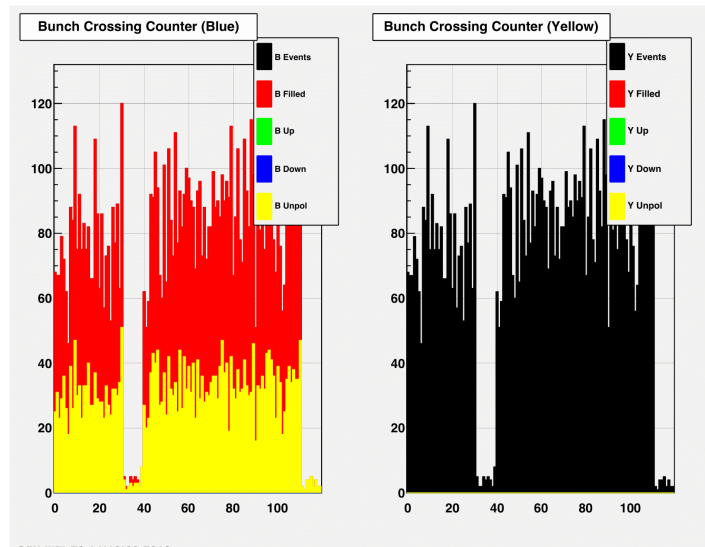


Figure 4.1: Bunch crossing distribution for run 16088023 as example. Left plot shows the blue beam bunch crossing distribution; right plot shows the yellow beam bunch crossing distribution. The abort gap for both blue beam and yellow beam are with bunch ID [31, 39] and [111, 119].



199 side RP track and only one west side RP track, while Figure (4.2 bottom) shows  
 200 another channel requiring only one east side RP track and only one west side RP  
 201 track. Channels other than the 2 acceptable cases are not considered because  
 202 they might contain background noise or pile-up events.

203 The next step is to identify if the RP tracks are good tracks. First of all, the  
 204 RP track needs to hit at least 7 silicon planes. According to the RP design, there  
 205 are 2 sets of RP (inner and outer) on each side. Each set contains a package  
 206 above and below the beamline. Each package contains 4 silicon planes, where  
 207 2 of them are used to determine the hit position in x direction and the rest 2  
 208 are used to determine the hit position in y position direction. The requirement  
 209 of RP track hitting at least 7 silicon planes will make sure not only the RP  
 210 track hits both packages, but also the hit position and track momentum can  
 211 be reconstructed more precisely. In addition, this cut can reduce the RP tracks  
 212 from background noise significantly, since a large number of background tracks  
 213 hit less than 4 silicon planes.

214 Then, the cuts on the polar angle of the RP tracks in the x-z plane ( $\theta_x$ ) and  
 215 y-z plane ( $\theta_y$ ) are applied to make sure the RP tracks are good reconstructed  
 216 tracks. The ranges of the cuts are obtained from the RP track  $\theta_x$  and  $\theta_y$  distri-  
 217 bution in both simulation and data. The simulation is based on RP, using the  
 218 Pythia8 + GEANT4 simulation framework. The details of the RP simulation  
 219 and the description of the cuts from the simulation are in Appendix (A). Figure  
 220 (4.3) show the only east side RP track  $\theta_x$  (left plot) and  $\theta_y$  (right plot) for data  
 221 with the cut on the number of silicon planes that RP track hit, and Figure (4.4)  
 222 show the only west side RP track  $\theta_x$  (left plot) and  $\theta_y$  (right plot) for data with  
 223 the cut on the number of silicon planes that RP track hit.

## 224 4.4 Background cut

225 There are quite a large number of pile-up events in data, which have a serious  
 226 impact on measuring the diffractive EM-jet  $A_N$  precisely. To deal with this  
 227 effect, two additional sets of cuts are applied to minimize the pile-up effect.

228 The first set of cuts is based on the sum of west side RP track energy  
 229 and EM-jet energy (sum energy). As shown in Figure (4.2), both possible  
 230 channels contain only one west side RP track and EM-jets at FMS. In addition,  
 231 the accidental coincident events usually have the sum energy greater than the  
 232 proton beam energy, so it's a good idea to consider the cut based on the sum  
 233 energy. The cuts on the sum energy are varied by the different  $x_F$  regions,  
 234 where  $x_F$  is the scaling variable of the particle in the hadronic collision and  
 235 can be calculated as the EM-jet energy divided by the proton beam energy for  
 236 the FMS EM-jets. The cuts are based on the splitting of the two peaks for

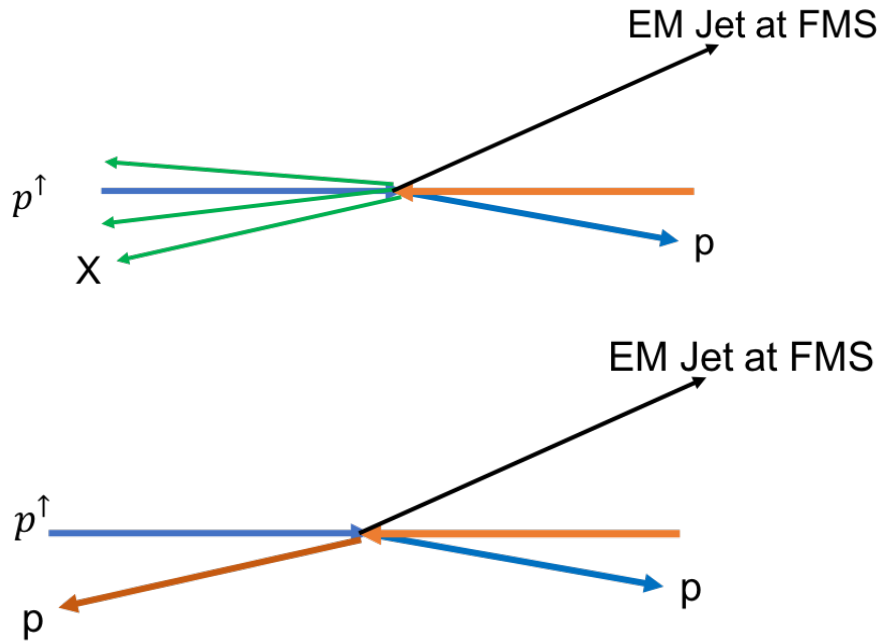


Figure 4.2: 2 possible channels for diffractive processes.

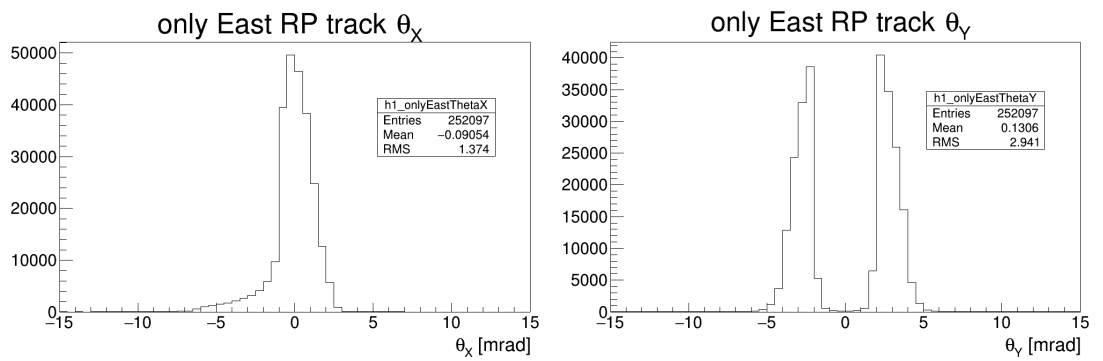


Figure 4.3: Distribution of the east side RP track  $\theta_x$  (left plot) and  $\theta_y$  (right plot)

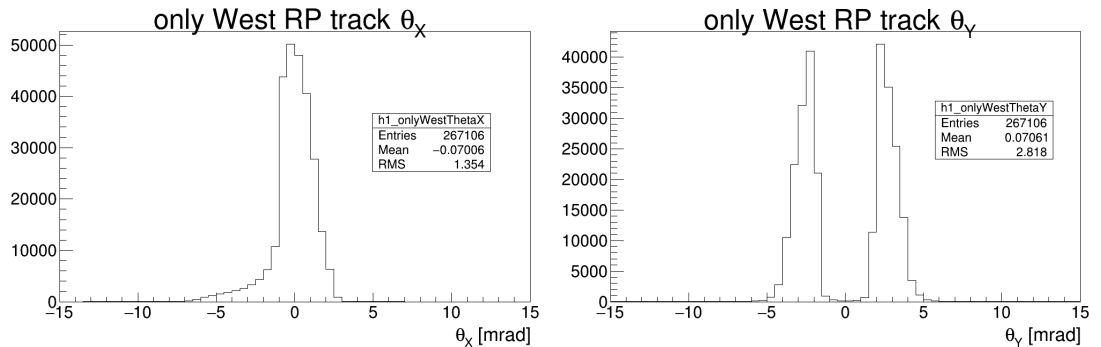


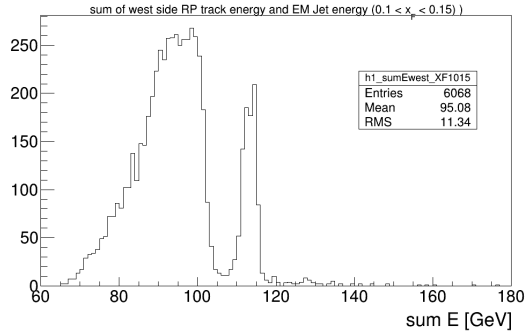
Figure 4.4: Distribution of the west side RP track  $\theta_x$  (left plot) and  $\theta_y$  (right plot)

Table 4.2: Sum energy cut for different  $x_F$  bins

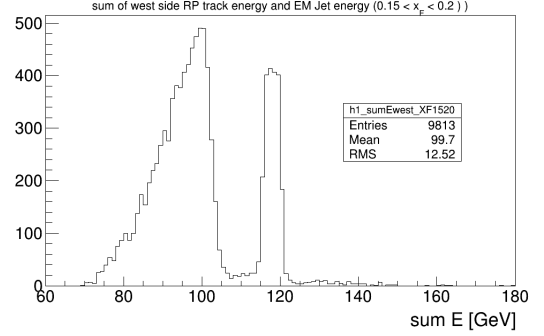
$x_F$	Sum energy [GeV]
[0.1, 0.15]	<108
[0.15, 0.2]	<108
[0.2, 0.25]	<110
[0.25, 0.3]	<110
[0.3, 0.45]	<115

237 each sum energy distribution (Figure (4.5)), where the peak with the lower sum  
 238 energy (close to beam energy, 100 GeV) is considered as the contribution from  
 239 the diffractive processes and the peak with the higher sum energy is considered  
 240 as the contribution from the pile-up events. Table (4.2) shows the sum energy  
 241 cuts for the EM-jets at each  $x_F$  region.

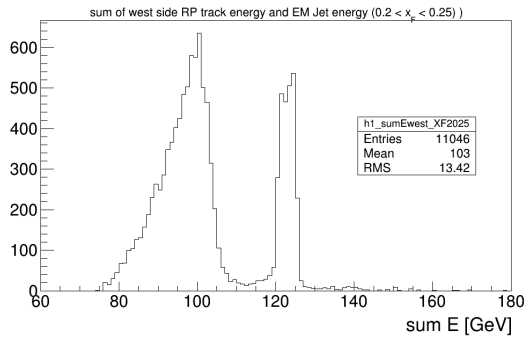
242 The second cuts are based on the Beam-Beam Counter (BBC), which is  
 243 used for triggering, luminosity monitoring and local polarization measurement  
 244 [?]. Generally, the pile-up events are more likely to appear in the high luminosity  
 245 collision. In addition, the higher luminosity detected in an event, the higher the  
 246 BBC ADC sum value will be collected. To decide the threshold of the BBC ADC  
 247 sum value from the event, the combination with sum energy cut is considered  
 248 to determine these cuts from BBC. In this analysis, only the west side BBC  
 249 detector responses are considered. Based on the BBC design, the BBC ADC  
 250 sum values from 2 different regions (small BBC and large BBC) are considered.  
 251 Figure (4.6) show the 2-dimension distribution of sum energy and west side  
 252 small (large) BBC ADC sum. To simplify, the events with sum energy less  
 253 than 108 GeV are considered signals while the events with sum energy greater  
 254 than 108 GeV are considered backgrounds. Also, to better qualify the cuts, the  
 255 ratios of signals to backgrounds by every BBC ADC sum bin are calculated and



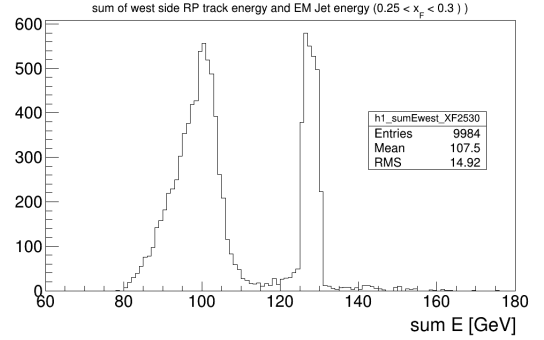
(a) Sum energy distribution for EM-jet with  $0.1 < x_F < 0.15$ .



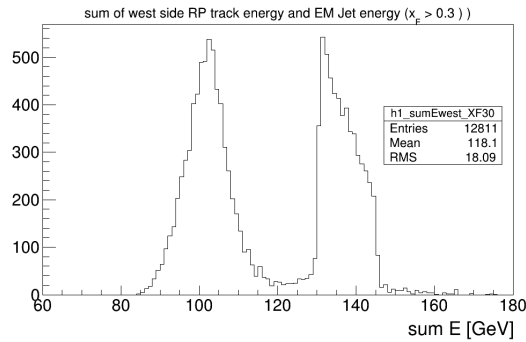
(b) Sum energy distribution for EM-jet with  $0.15 < x_F < 0.2$ .



(c) Sum energy distribution for EM-jet with  $0.2 < x_F < 0.25$ .



(d) Sum energy distribution for EM-jet with  $0.25 < x_F < 0.3$ .



(e) Sum energy distribution for EM-jet with  $0.3 < x_F < 0.45$ .

Figure 4.5: Sum energy distribution for EM-jet with  $0.1 < x_F < 0.45$ , but separate by 5 different  $x_F$  region.

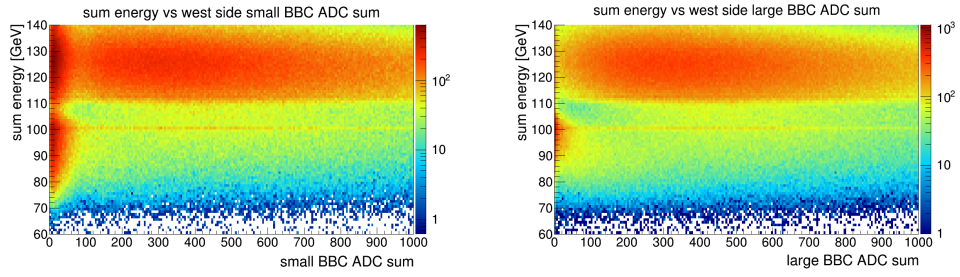


Figure 4.6: Distribution of sum energy vs west side small BBC ADC sum (left plot) and sum energy vs west side large BBC ADC sum (right plot). The region with sum energy  $> 108$  GeV is considered as background and the region with sum energy  $< 108$  GeV is considered as signal.

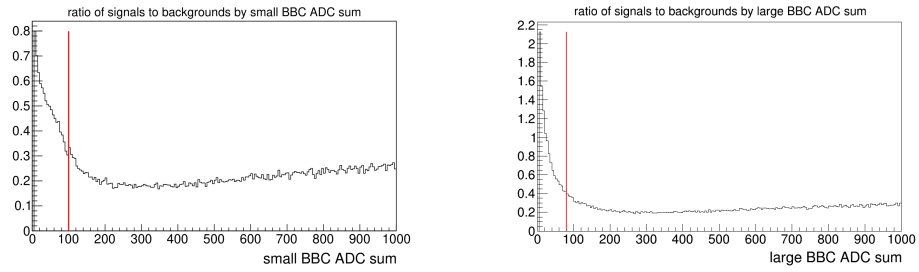


Figure 4.7: Distribution by every small BBC ADC sum bin (left) and by every large BBC ADC sum bin (right). The red vertical line indicate the proper cut for small (large) BBC ADC sum.

256 presented in Figure (4.7). From the figures, the west side small BBC ADC sum  
 257 cut is less than 100 and the west side large BBC ADC sum cut is less than 80.

## 258 Chapter 5

# 259 Corrections

### 260 5.1 Underlying Event (UE) correction

#### 261 5.1.1 Underlying Event energy correction for diffractive 262 process

263 The underlying event is a part of a jet, not from the parton fragmentation but  
264 from secondary scattering or other processes. This will deposit some energy to  
265 the jet, so the correction on UE is required to subtract the its energy (momen-  
266 tum) from the jet. The commonly used method is the "cross-ratio" method [19].  
267 In this method, first of all, two off axis jets with same pseudorapidity but at  
268  $\pm 1/2\pi$  azimuthal angle at the edge of the original jet are reconstructed as UE  
269 background. Then, the UE energy density can be calculated using  $\rho = E/(\pi R^2)$ ,  
270 where E is the UE energy and R is the UE jet radius. The fastjet program use  
271 the "ghost particle" technique to calculate the UE energy density ( $\rho$ ) and jet area  
272 (A). The maximum "ghost particle"  $\eta$  is 5.0 and the "ghost area" is 0.04. Finally,  
273 the jet energy will be subtracted by the UE energy:  $E_{corrected} = E_{original} - \rho \times A$ ,  
274 where the corrected EM-jet energy is  $E_{corrected}$  and the original EM-jet energy  
275 is  $E_{original}$ .

276 Figure (5.1) show the UE correction distribution for EM-jet energy. The left  
277 plot shows the subtraction term for the UE correction for EM-jet energy. The  
278 right plot shows the EM-jet energy distribution after the UE correction. If the  
279 EM-jet energy after subtraction is less than 0 GeV, the energy will be set to 0  
280 GeV.

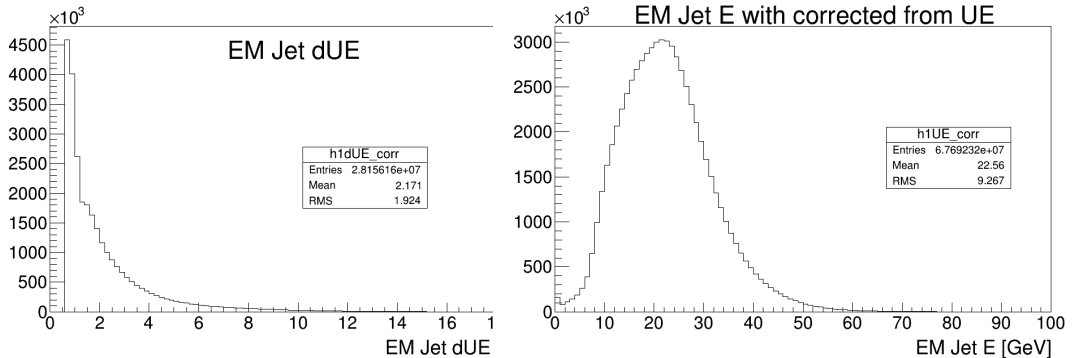


Figure 5.1: UE distribution for diffractive EM-jet analysis. The left plot shows the subtraction term  $\rho \times A$ . The right plot shows the EM-jet energy distribution after the UE correction.

### 281 5.1.2 Underlying Event energy correction for inclusive process 282

283 The UE correction for the inclusive process is similar to that for the diffractive  
284 process, but the correction object is the EM-jet transverse momentum instead  
285 of energy. The UE correction method, setup and procedures are the same as  
286 explained in Sec. (5.1.1). Since the correction object is the  $p_T$ , the calculation  
287 formula for EM-jet with UE correction is  $p_{T,corrected} = p_{T,original} - \rho \times A$ , where  
288 the corrected EM-jet  $p_T$  is  $p_{T,corrected}$ , the original EM-jet  $p_T$  is  $p_{T,original}$ ,  
289 UE  $p_T$  density is  $\rho$  and jet area is  $A$ , respectively.

## 290 5.2 Detector level to particle level EM-jet energy correction 291

292 The EM-jet energy obtained from FMS is considered detector level EM-jet en-  
293 ergy. Therefore, a correction for detector level to particle level EM-jet energy is  
294 necessary for both analyses. The correction is based on the Monte Carlo simulation  
295 for FMS. The details of the simulation are shown in (B). In the simulation,  
296 the EM-jets with both particle level and detector level are recorded. Figure ()  
297 shows the EM-jet energy distribution in particle level and detector level. In the  
298 plot, the black points are the correlation between the EM-jet energy in particle  
299 level and detector level. Then the polynomial functions are used to fit for the  
300 points in two different detector level regions:  $5 < E < 10$  GeV and  $10 < E < 60$   
301 GeV. The 6th-order polynomial function is used for the former region and the  
302 linear function is used for the latter region.

## 303 Appendix A

# 304 Roman Pot simulation

305 In Roman Pot simulation, PYTHIA8 generates the particle level events and  
306 GEANT4 is used for the RP detector level simulation.

307 The version of PYTHIA8 used in this analysis is 8.2.35 [17]. This Pythia  
308 version allows the simulation on diffractive process, including single diffractive,  
309 double diffractive and hard diffraction processes. In this analysis, we use the  
310 embedded Pythia in STAR database. The class for the embedded Pythia is  
311 "StarPythia8". The proton-proton collisions with  $\sqrt{s} = 200$  GeV are simulated.  
312 There are totally of 4 million events generated in the simulation. The single  
313 diffractive processes are selected to simulate the diffractive processes.

314 After PYTHIA simulation for particle level, GEANT 4 simulation with RP  
315 detector is applied in the detector level simulation. This RP simulation frame-  
316 work called "pp2pp" was developed by STAR Roman Pot group [18]. In this  
317 analysis, the 2015 geometry is used, where DX magnet and DX-D0 chamber are  
318 implemented specifically for Run 15. The particle level simulation results from  
319 PYTHIA 8 are used as the input for RP simulation.

320 After the simulation on RP, the RP tracks are checked. For the west side  
321 RP, figure (A.1) shows the number of silicon planes that the west side RP track  
322 hits; and figure (A.2) shows the number of silicon planes that the east side RP  
323 track hits. From the plot, if we choose to consider the global tracks which are  
324 the tracks hitting 2 RP packages, we should consider the tracks which hit more  
325 than 4 planes. Also, the tracks hitting 8 planes are dominant. For the data,  
326 therefore, the tracks hitting more than 6 planes will be considered to allow more  
327 reasonable statistics.

328 After that, the cut on RP tracks hitting more than 6 planes is applied when  
329 analyzing the simulation data. Figure (A.3) show the only east side RP track  
330  $\theta_x$  (left plot) and  $\theta_y$  (right plot), and Figure (A.4) show the only west side RP  
331 track  $\theta_x$  (left plot) and  $\theta_y$  (right plot). The distributions of either  $\theta_x$  and  $\theta_y$  are



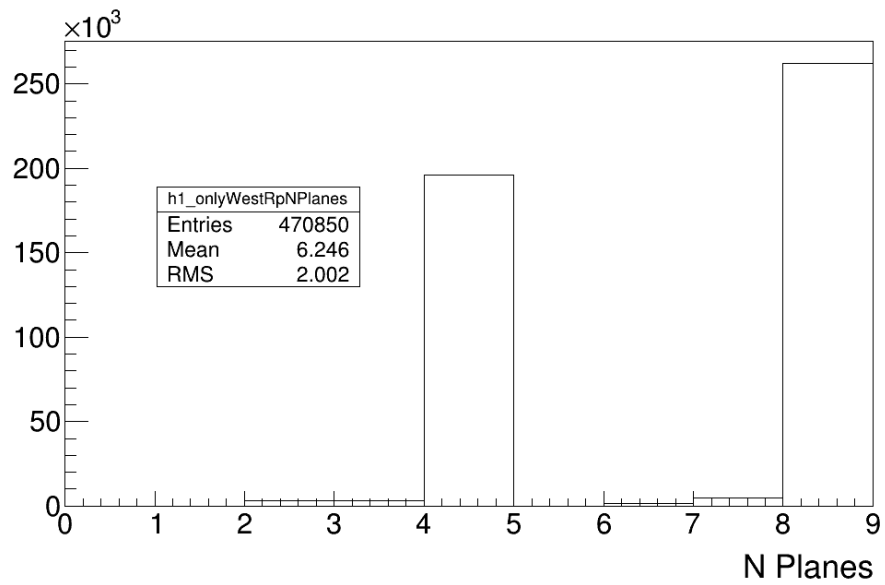


Figure A.1: Number of silicon planes that the west side RP track hits.

332 similar between the east side and the west side RP tracks. Therefore, the same  
 333 cuts based on  $\theta_x$  and  $\theta_y$  can be considered for both the east side and the west  
 334 side RP tracks:  $-2 < \theta_x < 2$  mrad and  $1.5 < |\theta_y| < 4.5$  mrad.

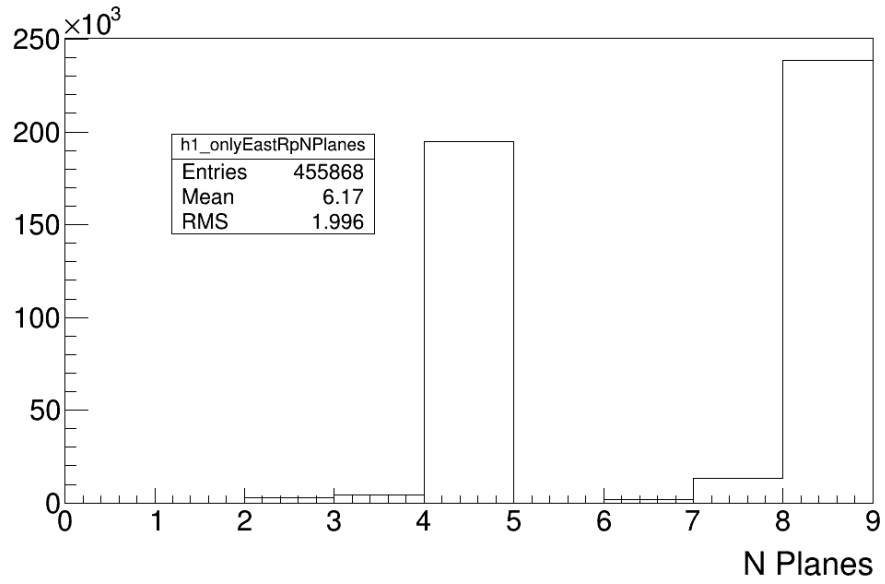


Figure A.2: Number of silicon planes that the east side RP track hits.

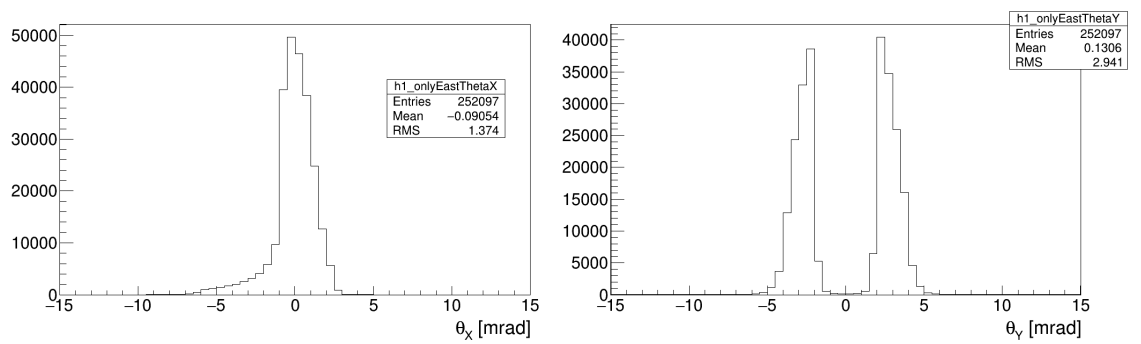


Figure A.3: Distribution of the only east side RP track  $\theta_x$  (left plot) and  $\theta_y$  (right plot)

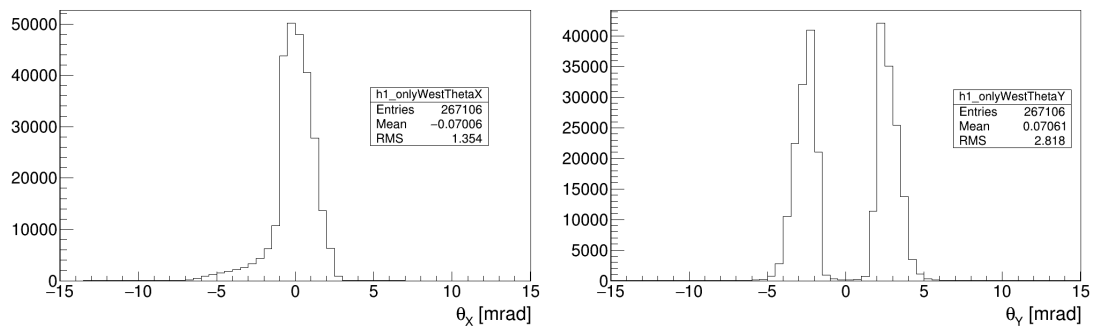


Figure A.4: Distribution of the only west side RP track  $\theta_x$  (left plot) and  $\theta_y$  (right plot)

## 335 Appendix B

### 336 FMS simulation

337 PYTHIA6 generates the particle level events in the simulation, and GEANT3  
338 is used for the FMS detector level simulation.

339 For the PYTHIA simulation, the proton-proton collisions with  $\sqrt{s} = 200$   
340 GeV are generated, with the tune setting of Perugia6 (Tune parameter 370)  
341 [20]. Then, the GEANT3 with FMS detector response implemented under  
342 STAR simulation framework ("starsim") are used for the FMS simulation. The  
343 Big Full Chain (BFC) proceeds for the event reconstruction. The chain option  
344 is "ry2015a agml usexgeom MakeEvent McEvent vfmce Idst BAAna l0 l3 Tree  
345 logger fmsSim fmspoint evout -dstout IdTruth bigbig fzin geantout clearmem  
346 sdt20150417.193427". The EM-jet reconstruction is proceeded along with the  
347 BFC process. The Anti- $k_T$  algorithm with  $R=0.7$  is used for the EM-jet re-  
348 construction, the same as the EM-jet reconstruction for data. Details of the  
349 EM-jet reconstruction are shown in 2.3. In addition, the event filter (StFmsFil-  
350 terMaker) and the trigger simulator (StFmsTriggerMaker) are applied during  
351 the BFC process. The former filter is based on the energy sum per FMS quad-  
352 rant, while the latter filter is based on the FMS trigger. Finally, those events  
353 passing the filter in the event level and the trigger are saved for both particle  
354 level and detector level.

# 355 Bibliography

- 356 [1] D.L. Adams *et al.*, Phys. Lett. B 261, 201(1991)
- 357 [2] B.I. Abelev *et al.* (STAR Collaboration), Phys. Rev. Lett. 101,  
358 222001(2008)
- 359 [3] A. Adare *et al.* Phys. Rev. D 90, 012006 (2014)
- 360 [4] E.C. Aschenauer *et al.*, arXiv:1602.03922
- 361 [5] J. Adam *et al.* (STAR Collaboration), Phys. Rev. D 103, 092009 (2021)
- 362 [6] G. L. Kane, J. Pumplin, and W. Repko. Phys. Rev. Lett. 41, 1689 (1978)
- 363 [7] D. Sivers, Phys. Rev. D 41, 83 (1990)
- 364 [8] J. Collins, Nucl Phys B 396 (1993) 161
- 365 [9] J.W. Qiu and G. Sterman, Phys. Rev. Lett. 67 2264 (1991)
- 366 [10] M.M. Mondal (STAR Collaboration) PoS (DIS2014) 216
- 367 [11] V. Khachatryan *et al.* (CMS Collaboration) Phys. Rev. D 92, 012003 (2015)
- 368 [12] Z. Zhu, [https://drupal.star.bnl.gov/STAR/system/files/AnalysisNote\\_0601\\_0.pdf](https://drupal.star.bnl.gov/STAR/system/files/AnalysisNote_0601_0.pdf)
- 369 [13] M.Cacciari, G. P. Salam, and G. Soyez, Eur. Phys. J. C (2012) 72: 1896
- 370 [14] C. Kim, [https://drupal.star.bnl.gov/STAR/system/files/fmsCalib\\_0.pdf](https://drupal.star.bnl.gov/STAR/system/files/fmsCalib_0.pdf)
- 371 [15] C. Kim, [https://drupal.star.bnl.gov/STAR/system/files/note\\_9.pdf](https://drupal.star.bnl.gov/STAR/system/files/note_9.pdf)
- 372 [16] [https://drupal.star.bnl.gov/STAR/blog/oleg/spin-patterns-and-](https://drupal.star.bnl.gov/STAR/blog/oleg/spin-patterns-and-polarization-direction)  
373 [polarization-direction](https://drupal.star.bnl.gov/STAR/blog/oleg/spin-patterns-and-polarization-direction)
- 374 [17] T. Sjöstrand *et al.*, arXiv:1410.3012
- 375 [18] [https://drupal.star.bnl.gov/STAR/system/files/LFS\\_UPCGeant4SimulationOfRomanPots\\_17October](https://drupal.star.bnl.gov/STAR/system/files/LFS_UPCGeant4SimulationOfRomanPots_17October)
- 376 [19] B. B. Abelev *et al.* (ALICE Collaboration), Phys. Rev. D 91, 112012 (2015)
- 377 [20] P. Skands, arXiv:1005.3457